

# Elastic and attenuation anisotropy in directionally solidified (hcp) zinc, and the seismic anisotropy in the Earth's inner core

Michael I. Bergman<sup>\*</sup>, Louis Giersch, Michael Hinczewski, Valerie Izzo

*Physics Department, Simon's Rock College, 84 Alford Rd, Great Barrington, MA 01230, USA*

Received 3 November 1998; accepted 6 April 1999

## Abstract

The inner core of the Earth has been interpreted as being elastically anisotropic, with the direction parallel to the rotation axis fast. There are also observations that north–south rays exhibit greater amplitude reduction and more complex waveforms. In previous work, we found that directionally solidified, polycrystalline, tin (Sn)-rich alloys exhibit a solidification texturing that is measurable ultrasonically, and suggested that such texturing might be a cause for the observed seismic elastic anisotropy. Here, we find that zinc (Zn)-rich alloys also exhibit a measurable elastic anisotropy that is due to a preferred growth direction. We confirm the grain orientation by back-reflection X-ray diffraction. Zn solidifies as a hexagonal closest-packed (hcp) metal, albeit one with a  $c/a$  ratio greater than the ideal, unlike hcp iron (Fe), and is 60% elastically anisotropic. We also find that the columnar dendritic grains that grow with a preferred orientation during directional solidification result in anisotropic scattering off grain boundaries, yielding an anisotropic apparent attenuation. In addition, we present results for directionally solidified 100% Zn, which exhibits qualitative differences in both the elastic and attenuation anisotropy from Zn alloys. The laboratory results can be interpreted as a cause for both the seismic elastic and attenuation anisotropy if the cooling near the inner core has more nearly cylindrical than spherical symmetry. © 2000 Elsevier Science B.V. All rights reserved.

*Keywords:* Seismic elastic anisotropy; Solidification; Symmetry

## 1. Introduction

In recent years, there has been considerable interest in the elastic and attenuation properties of the Earth's inner core. Morelli et al. (1986) and Woodhouse et al. (1986) inferred from seismic body waves

and free oscillations, respectively, that the inner core of the Earth is elastically anisotropic, with the fast direction parallel to the rotation axis. Creager (1992) and Tromp (1993) confirmed these results, and much subsequent work has gone into determining details of the geographic distribution of the anisotropy (for a review, see Song, 1997).

There is also evidence for an attenuation anisotropy that is correlated with the elastic anisotropy, i.e., body waves traversing the inner core parallel to the rotation axis generally exhibit more complex waveforms and greater amplitude attenuation, by a factor

<sup>\*</sup> Corresponding author. Tel.: +1-413-528-7432; fax: +1-413-528-7365; e-mail: bergman@simons-rock.edu

of three to five, than those perpendicular to the rotation axis (Creager, 1992; Song and Helmlinger, 1993; Souriau and Romanowicz, 1997; Cormier et al., 1998). In addition to the attenuation anisotropy, it has been observed that the overall attenuation of compressional waves in the inner core is high, particularly near the top (Bhattacharyya et al., 1993). This high bulk anelasticity might result from a mushy zone (see Section 2) beneath the inner–outer core boundary that still contains interdendritic pockets of Fe alloy that have not yet solidified (Loper and Fearn, 1983). Such a scenario leads naturally to more attenuation near the top of the inner core where more interdendritic melt remains.

Several suggestions have been put forth to explain the net elastic anisotropy of the inner core, all invoking elastic anisotropy of the individual Fe grains that compose the inner core and some means of aligning the crystal axes. Under inner core conditions Fe is often thought to be hexagonal closest-packed (hcp) (Shen et al., 1998), though some studies indicate a double hexagonal closest-packed (dhcp) structure (Saxena et al., 1996). The elastic properties of this dhcp phase are not known, though its symmetry is similar to that of hcp Fe.

The means of aligning the crystal axes fall broadly into two classes: texturing frozen-in during solidification, and post-solidification texturing due to solid-state flow. The latter includes deformation texturing resulting from thermally driven solid-state free convection (Jeanloz and Wenk, 1988), recrystallization or deformation texturing resulting from solid-state poloidal flow (dominated by Legendre polynomial  $P_{20}$  radial flow and  $P_{21}$  latitudinal flow) driven by the equilibrium solidification surface being more oblate than the gravitational equipotential due to the rotationally dominated pattern of convection in the outer core (Yoshida et al., 1996), and a recrystallization or deformation texturing due to a solid-state mean toroidal flow (component  $T_{10}$ ) driven by a longitudinally asymmetric, super-rotating inner core responding to mass inhomogeneities in the mantle (Buffett and Creager, 1998). The former includes solidification texturing and columnar crystal growth with cylindrical symmetry also due to the primary role of the Coriolis force in the outer core (Bergman, 1997), paramagnetic texturing of crystals during solidification in a magnetic field (Karato, 1993), and

no texturing because the inner core is a single crystal (Stixrude and Cohen, 1995).

Each mechanism has its drawbacks as an explanation for understanding inner core observations. Firstly, it is not clear whether the inner core is undergoing free convection (Yukutake, 1998), why the convection should be aligned with the rotation axis (unless it is additionally influenced by outer core convection), whether the strain rates would be large enough to cause a significant texture to develop, or whether the primary slip planes of hcp Fe would yield a deformation texture with the correct sense (Poirier and Price, 1998). Similarly, the strain rates due to solid-state flow driven by preferential equatorial solidification may not be large enough to yield a sufficiently textured inner core, though the longer time available for deformation at smaller radii could lead to the observed depth dependence (Yoshida et al., 1996). Further, if the slip planes of hcp Fe are primarily basal rather than prismatic (Poirier and Price, 1998), the  $P_2$  flow may not lead to the proper texture, an issue also with a mean  $T_{10}$  flow.

Cylindrical growth of columnar dendritic crystals can yield the correct sense and depth dependence of the elastic anisotropy in the inner core (Bergman, 1997), as well as its bulk attenuation and anisotropy (Bergman, 1998; Cormier et al., 1998), and in this study we show that solidification texturing and anisotropic attenuation in directionally solidified hcp alloys does occur. In order for the inner core to maintain its nearly spherical shape, this mechanism presumably occurs in conjunction with a  $P_2$  flow that could change the original solidification texture (which has always been assumed to be isotropic in deformation models). Paramagnetic texturing has not been demonstrated in directionally solidified metals or alloys, so that it is difficult to evaluate its relevance to the inner core. Finally, if the single crystal elastic anisotropy of hcp Fe is greater than 4% (Bergman, 1998), and given recent seismic interpretations of a more complex pattern of inner core anisotropy, it would seem that the inner core cannot behave elastically as a single crystal. In any case, all mechanisms must invoke some sort of positive feedback, or mantle control, which requires an inner core that is not super-rotating, to explain longitudinal variations in the strength of the anisotropy.

## 2. The origin of elastic and attenuation anisotropy in directionally solidified metals

In a typical casting, random nucleation along the chill surface yields an equiaxed chill zone composed of crystals with all orientations and no shape anisotropy. Those grains with a favorable orientation for growth move ahead of their neighbors in the chill zone, producing the columnar zone composed of crystals elongated in the direction of heat flow and with a preferred orientation (Porter and Easterling, 1992).

For directionally solidified pure metals the interface between the solid and the melt, though atomically diffuse, is macroscopically smooth, and it is observed that the preferred texture that develops in the growth direction is  $\langle 001 \rangle$  (Miller–Bravais indices  $\langle 0001 \rangle$ , also known as the  $c$ -axis) in hcp metals (Hellowell and Herbert, 1962). For metallic alloys constitutional supercooling can result in a macroscopically corrugated solid–metal interface where non-faceted dendrites grow away from the solid and form a mushy zone. The preferred crystallographic direction of dendritic crystal growth is  $\langle 210 \rangle$  (Miller–Bravais indices  $10\bar{1}0$ ) in hcp metals (Hellowell and Herbert, 1962). Fig. 1 is a schematic of crystal growth in directionally solidified metallic alloys, showing dendritic columnar crystals. It has been proposed that the inner core is growing dendrit-

ically, and that at least the upper part is still in a mushy state where interdendritic melt remains (Fearn et al., 1981).

Non-faceted dendritic growth is common in both water-rich and salt-rich aqueous solutions, and certain organic systems, as well as metallic alloys. It is less common in silicates, which tend to have atomically flat and macroscopically faceted solid–melt interfaces (Porter and Easterling, 1992). The same solidification textures that are observed in pure hcp metals and hcp metallic alloys are also observed in ice, which is hcp. As with pure hcp metals, lake ice generally grows with vertical  $c$ -axes, i.e., the  $c$ -axes parallel to the growth direction, though the preferred orientation of lake ice can be sensitive to seeding (Gow, 1986). The crystals of the columnar zone tend to be irregularly shaped and massive, often over a meter in transverse cross-sectional area in New England lakes. Sea ice, which grows dendritically (actually, by platelets, which represent the fast-growing basal planes), always exhibits horizontal  $c$ -axes in the columnar zone beyond the initial ice skim (Weeks and Gow, 1978). As in metallic alloys, the dendritic crystals exhibit a strong shape anisotropy, being elongated in the growth direction.

Transverse to the solidification growth direction there is typically no preferred orientation, so that columnar grains can be oriented arbitrarily about the crystallographic axis of growth (Fig. 2). Bergman

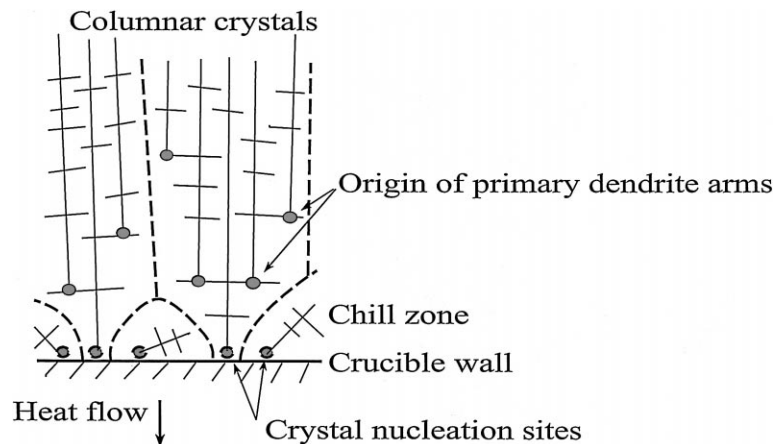


Fig. 1. The structure of a directionally solidified metallic alloy, showing randomly oriented, equiaxed chill zone beneath the dendritic, columnar zone. The dendrites parallel to heat flow have a growth advantage, and since they grow in a particular crystallographic direction, a preferred orientation results. After Porter and Easterling (1992).

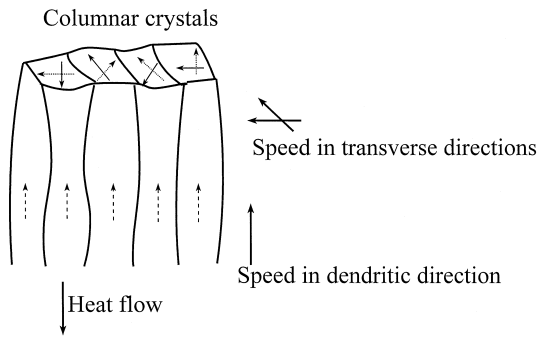


Fig. 2. Transverse to the growth direction grains can be oriented arbitrarily, so that there is more likely to be an impedance contrast between grains transverse to growth than parallel to growth.

(1998) suggested this arbitrary rotation of elongated grains about the growth direction might yield anisotropic elastic scattering, and thus an anisotropic apparent attenuation, because waves propagating transversely to the growth direction cross more grain boundaries with non-zero impedance contrasts than waves propagating parallel to the growth direction. In particular, in hcp alloys the growth direction is  $\langle 210 \rangle$  so that in the transverse direction grains can be oriented anywhere in the  $\langle 010 \rangle$ – $\langle 001 \rangle$  (Miller–Bravais indices  $\langle 1\bar{2}10 \rangle$ – $\langle 0001 \rangle$ ) plane, which is not isotropic. We will show ultrasonic results for directionally solidified Zn that bear out this prediction.

Previous work on apparent attenuation due to scattering of ultrasonic elastic waves has been mostly concerned with the frequency dependence of the scattering, assuming no preferred orientation is present and the grain shape is isotropic (Mason and McSkimin, 1948; Roth, 1948). These studies examined the effect of grain size  $d$  vs. wavelength  $\lambda$ , in the Rayleigh scattering limit where  $\lambda \gg d$  and the scattering is proportional to  $d^3$ , and the reflection limit where  $\lambda \ll d$  and the scattering is proportional to  $d^{-1}$ . There have also been a few experimental studies on the effects of preferred orientation on scattering. For instance, the  $\langle 210 \rangle$  axis in drawn Zn lies along the bar axis and, as in directionally solidified Zn, the  $\langle 010 \rangle$  and  $\langle 001 \rangle$  axes are oriented arbitrarily in the transverse (radial) plane. In such bars, Papadakis (1968) found the apparent attenuation in the radial direction exceeded that in the axial direction by a factor of six, presumably due to anisotropic scattering. He also discussed the possibil-

ity that for grains with significant shape anisotropy the magnitude of  $\lambda/d$  could be different in different directions.

### 3. Experimental procedure

Although there have been X-ray diffraction studies of solidification texturing in directionally solidified metals (Hellawell and Herbert, 1962), there have been no ultrasonic studies other than Bergman (1997), on Sn-rich tetragonal alloys. Moreover, there have been no studies of anisotropic apparent attenuation caused by a preferred orientation due to solidification. Metals such as titanium and zirconium at atmospheric pressure that are thought to be good analogs for high-pressure hcp Fe (Jeanloz and Wenk, 1988) transform to the body-centered cubic phase before melting, so that they are not suitable for a study of the solidification of hcp metals. Although its  $c/a$  ratio (1.86) is on the opposite side of the ideal (1.63) from that expected for hcp Fe (1.60, Stixrude and Cohen, 1995), Zn is hcp at all temperatures beneath its melting temperature. It is also relatively easy to work with, and its 60% elastic anisotropy makes it ideal for this ultrasonic study.

A variety of Zn-rich Sn alloys were examined (Table 1), varying from 0 to 10 wt.% Sn. The system has a simple eutectic phase diagram (Fig. 3), and is representative of an alloy phase diagram when a solid miscibility gap exists. The presence of Sn promotes constitutional supercooling, but the percent Sn is low enough that the interdendritic Sn-rich phase, which has a typical lengthscale of 10  $\mu\text{m}$ , does not substantially alter the ultrasonic results. This small mass percent of interdendritic solute-rich phase within the larger crystals of the solvent-rich phase is likely similar to the Earth's core (Jephcoat and Olson, 1987) where compositional convection carries the lighter solute out of the inner core mushy zone (Bergman et al., 1997). We prepared 400 g, 35 mm diameter ingots of the various compositions from 99.99% purity Zn and Sn, which were melted in a resistance furnace with the heating coils near the top, a water chill at the bottom, and sidewall insulation. The melts were cooled at a programmed rate, with a type-K thermocouple in the graphite crucible wall near the top of the melt column providing

Table 1

Measured longitudinal wavespeeds (km/s)  
Compressional wavespeeds (km/s) in the growth direction and each transverse direction for each solidification condition. The speeds are computed from the travel times. When possible, two speeds are given, one for the first echo and a second for the second echo. For the top cube cut from the 100% Zn ingot, two widely different speeds are found in the growth direction depending on the location of the transducer (see text). The speeds in the square brackets are the speeds in the growth direction in the top cubes predicted by averaging the speeds in the growth direction of the grains whose orientation is known from the X-ray diffraction data, and using Fig. 9.

	Growth direction	Transverse direction 1	Transverse direction 2
Top, 100% Zn	2.97 (4.41)	4.43	4.52
1.5°C/min	– (4.51)	4.52	4.61
(Cube A)	[3.03] ([4.60])		
Bottom, 100% Zn	–	4.51	4.59
1.5°C/min (B)	–	4.62	4.68
Top, 97% Zn	4.59	4.09	4.20
0.75°C/min (C)	4.55 [4.68]	–	–
Bottom, 97% Zn	4.43	4.12	4.11
0.75°C/min (D)	–	–	–
Top, 97% Zn	4.50	4.08	4.18
1.5°C/min (E)	4.52 [4.60]	–	–
Bottom, 97% Zn	4.43	3.90	4.09
1.5°C/min (F)	–	–	–
Top, 97% Zn	4.50	4.30	4.02
1.5°C/min (G)	4.61 [4.60]	–	–
Bottom, 97% Zn	4.41	4.12	4.34
1.5°C/min (H)	–	–	–
Top, 97% Zn	4.51	4.13	4.15
2.5°C/min (I)	4.60 [4.72]	–	–
Bottom, 97% Zn	4.37	3.94	3.92
2.5°C/min (J)	–	–	–
Top, 90% Zn	4.26	4.10	3.92
1.5°C/min (K)	–	–	–
Bottom, 90% Zn	4.25	3.94	3.89
1.5°C/min (L)	–	–	–

feedback to a microprocessor. A second passive thermocouple near the base of the crucible gave information about the vertical temperature gradient. The water chill provided a temperature gradient that decreased as the overall temperature of the furnace decreased. The solidified ingots slipped easily out of the graphite crucible, and the crucible was reused.

After solidification the approximately 6 cm tall ingots were chemically etched in 100% HCl to reveal the grain boundaries on the ingot surface. Two 2 cm per edge cubes were cut from each ingot, one a few millimeters above the bottom, the second from

just below the top. Opposite cube faces were machined parallel to 1/1000 in. (25  $\mu\text{m}$ ), and these were then ground and polished flat to 1  $\mu\text{m}$ . Chemical etching again revealed the grain boundaries so that grain-by-grain back-reflection X-ray diffraction (the Laue method) could be carried out. The Laue method is used to determine the orientation of a single crystal, but we used it here for a polycrystalline sample where the grains are typically larger than the X-ray beam width.

We directed the incident X-ray beam parallel to the direction of growth, and for a set of reflection planes within the crystal that satisfies the Bragg condition for some wavelength in the X-ray spectrum, the radiation is back-scattered towards the photographic film. The Laue spots on the film correspond to those families of planes with normals closest to the direction of the incident X-ray beam. A given Laue spot can be used to determine the normal of the corresponding set of planes because the normal bisects the angle between the reflected beam that causes the spot and the incident beam (which is directed through the center and normal to the photographic film). Using a tungsten target to provide the full X-ray spectrum, we found that 15 mA at 30 kV for 6 min led to a good exposure.

Planes parallel to an axis of some crystallographic direction, known as the zone axis, form what is known as a zone, and these planes reflect beams along the surface of a cone. The axis of the cone is the zone axis and the cone intersects the film in a hyperbola or straight line (in the special case that the zone axis is perpendicular to the incident beam). These zone hyperbolae are clearly distinguishable in

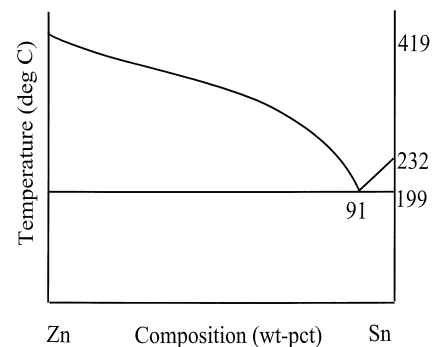


Fig. 3. Zn–Sn phase diagram (Smithells, 1949).

the pattern of individual Laue spots on the photograph. Using a Greninger chart, the hyperbolae can be plotted as great circles on a stereographic projection. The zone axes, which lie  $90^\circ$  from the great circles, and the poles at the intersection of the plotted great circles, are usually axes of high symmetry, and so correspond to planes of low index. The angles between all of the poles and zone axes can then be measured on the stereographic projection until each can be positively identified by comparison with the known angular separations. Using the Greninger chart one can then read the angular coordinates between the incident X-ray beam (in this case, the growth direction) and the now indexed Laue spots. For further details of the method, see Cullity (1978).

Assuming the identification is correct, the only error in determining the grain orientation is introduced at this last step, where we estimate the recorded error is  $\pm 1^\circ$ . This error is due to the spots not being precisely points (perhaps due to deformation during polishing) and to the  $2^\circ$  grid of the Greninger chart. Only those photographs clear enough and containing a sufficient number of spots to make a positive identification were used. For the bottom face of most cubes, we determined the orientation of at least four grains, and the results of both cubes for all ingots were plotted on an inverse pole figure, which shows the distribution of the growth direction relative to the crystal axes. Although the grains whose orientation were found and plotted naturally show a bias towards being larger, these grains comprise a greater volume of the ingot and will be primarily responsible for an overall elastic anisotropy.

We then studied propagation of ultrasonic compressional waves in the cubes. Using the Matec Instruments TB-1000 Gated Amplifier Toneburst Plug-in Card, we carried out the pulse–echo technique (McSkimin, 1950). We used a general purpose, commercial P-wave transducer, 0.375 in. in diameter, with a fundamental frequency at 5.0 MHz. The transducer was coupled to the cube, without a buffer, using industrial ultrasonic couplant (Sonotech). The pulse width was typically in the range 1–3  $\mu\text{s}$  and the repetition rate was 13 ms, and the resulting echoes were recorded digitally off of an oscilloscope using Lab View. An algorithm was developed to systematically pick the travel time of a pulse. Essentially, as an indication of the arrival of a

pulse we required two consecutive points in the time series to have amplitude values larger than some preset value. An estimate of the uncertainty in travel time can be obtained by assuming the possibility that the algorithm is mispicking the time by one cycle. For the cubes of 100% Zn, in which the cross-sectional area of the columnar grains tends to be larger than in alloys, measurements of travel time parallel to the growth direction were somewhat sensitive to the transducer position, because one is more likely to be measuring the travel time in a single crystal rather than an average. For each travel time we then calculated the compressional wavespeed and the uncertainty, knowing the cube thickness.

It is more difficult to be quantitative about attenuation because of issues such as geometric spreading, sidewall reflections, transducer size and shape relative to the sample, non-constant transducer/sample bond, wearplates on commercial transducers, and excessive energy transfer between the sample and the transducer during echo impingement, which leads to a high apparent attenuation (Papadakis, 1990). However, by keeping the cube geometry and transducer constant, we can at least make observations on the relative attenuation between different cubes and directions. In this study, we will simply show the waveforms, which strongly suggest an apparent attenuation anisotropy that is due to anisotropic scattering due to the preferred texturing of the columnar crystals.

#### 4. Results

Fig. 4 shows a slice of the exterior surface of a 3 wt.% Sn–Zn ingot cooled at  $1.5^\circ\text{C}/\text{min}$ . As in Fig. 1, the equiaxed chill zone (where the grains have no strong shape anisotropy) is at the bottom of the ingot, with the columnar zone above. The primary dendrites appear as the series of parallel lines within each grain. From crystal to crystal they are typically at a small angle to each other, but they tend to lie within  $15^\circ$  of the growth direction. This is a macroscopic indication that the ingot is textured. The dendrites are visible due to solidification shrinkage, with the Sn-rich phase present interdendritically. Fig. 5 shows the exterior surface of a 100% Zn ingot cooled at the same rate. The columnar nature of the



Fig. 4. A chemically etched, exterior slice of a 3 wt.% Sn–Zn ingot directionally solidified at 1.5°C/min. The dendrites that comprise the columnar crystals can be seen because of solidification shrinkage. Compare with Fig. 1.

ingot is again obvious, but the grains tend to be larger, with smoother macroscopic boundaries, and the grains are not dendritic. Figs. 6 and 7 show the grain boundaries in transverse and longitudinal sections of the 100% Zn upper cube, after etching.

Fig. 8 is an inverse pole figure for grains from cubes cut from the ingots listed in Table 1. It is apparent that, as expected, the growth direction tends to be  $\langle 001 \rangle$  for 100% Zn, and within  $30^\circ$  of  $\langle 210 \rangle$  for the Zn alloys. The exceptions are a few grains from the bottom face of a couple of bottom cubes that are not growing in a low index direction, perhaps because these grains are still within the chill zone, and one grain nearer the top of a 100% Zn ingot that is growing about  $25^\circ$  from the  $\langle 210 \rangle$  direction. There is no obvious trend in the degree of texturing as a function of cooling rate, within the limited range of cooling rates and number of grains

that we have studied, nor does the 10 wt.% Sn–Zn alloy show different texturing than the 3 wt.% Sn–Zn alloys.

Fig. 9 shows the Zn single crystal longitudinal wavespeed vs. direction from the  $c$ -axis (Simmons and Wang, 1971). It can be seen that the basal plane is faster than the  $c$ -axis, opposite that expected for hcp Fe (Stixrude and Cohen, 1995; Bergman, 1998). Table 1 and Fig. 10 give our ultrasonic results. The estimated uncertainty is about  $\pm 0.08$  km/s. In Fig. 10, we also indicate the speeds predicted for 100% Zn and 3 wt.% Sn–Zn assuming the solidification texturing is complete.

For comparison, we have also included the speed in the growth direction in each of the top cubes predicted by averaging the speeds in the growth direction of the grains whose orientation is known from Fig. 8, and using Fig. 9 (though it is not clear

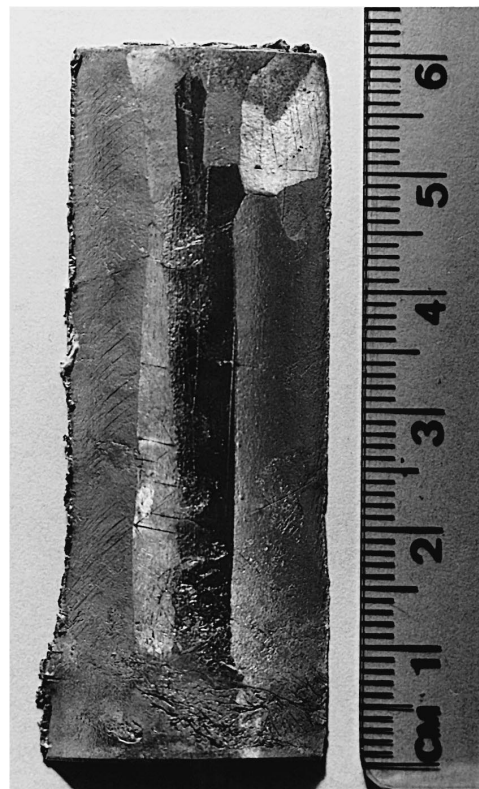


Fig. 5. A chemically etched, exterior slice of a 100% Zn ingot directionally solidified at 1.5°C/min. The columnar crystals are not dendritic, and tend to be larger than in the alloy.



Fig. 6. A chemically etched transverse section of a cube cut from the top of a 100% Zn ingot.

that a simple average is appropriate since the columnar grains are more nearly being sampled in parallel rather than in series). We do not include predictions for the bottom cubes because the X-ray data is for the bottom face of the cubes, in or near the chill zone, which may not be representative of the cube as a whole (which is why there is scatter in the orientation of the grains in the bottom cubes, but the ultrasonic measurements, which sample the whole cube, yield more consistent results). We also did not predict results for cubes with 10 wt.% Sn because the higher Sn content begins to significantly slow the speeds from that of 100% Zn.

For the alloys (cubes C–L in Fig. 10), we were often able to measure the travel time of multiple echoes in the growth direction because the pulses stood out clearly (Fig. 11, top). In contrast, in the two transverse directions, we were able to measure only the travel time of the first echo because it was not possible to see clearly subsequent pulses (Fig. 11, bottom). The growth direction is consistently faster than the transverse directions (Fig. 10). This is in accordance with the predicted solidification tex-



Fig. 7. A chemically etched longitudinal section of a cube cut from the top of a 100% Zn ingot, showing the columnar grains.

ture that was observed using X-ray diffraction. The growth direction in Zn alloys is predicted to be  $\langle 210 \rangle$ , with a wavespeed of 4.75 km/s (Fig. 9). The observed speeds in this direction are somewhat slower

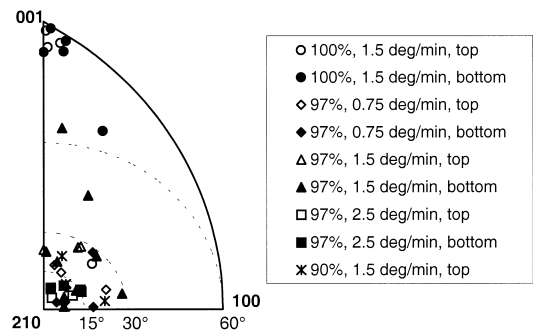


Fig. 8. An inverse pole figure for grains from the bottom face of bottom and top cubes cut from pure and alloy ingots cooled at various rates. The points plotted represent the growth direction. Open symbols, top cubes; filled symbols, bottom cubes. Circles, 100% Zn, cooled at 1.5°C/min; diamonds, 97% Zn, 0.75°C/min; triangles, 97% Zn, 1.5°C/min; squares, 97% Zn, 2.5°C/min; asterisks, 90% Zn, 1.5°C/min (top cube only).

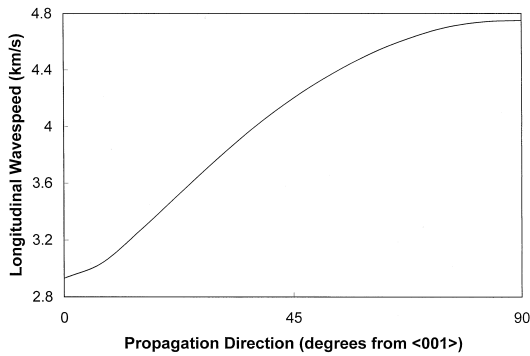


Fig. 9. Compressional wavespeed for Zn in the  $\langle 001 \rangle$ – $\langle 210 \rangle$  plane (Simmons and Wang, 1971).

than this value, indicating incomplete texturing. Similarly, in the transverse directions the observed speeds are in most cases slightly faster than the 4.02 km/s expected for grains oriented arbitrarily in the  $\langle 010 \rangle$ – $\langle 001 \rangle$  plane.

The speeds in the growth direction predicted by the X-ray diffraction data are consistently slightly faster than the observed speeds, even accounting for

the 0.08 km/s uncertainty in the ultrasonic measurements and the small uncertainty in the grain orientation. This may be due to a bias towards larger grains in the selection of grains whose orientation we found. These larger grains are perhaps more likely to be oriented with the fast  $\langle 210 \rangle$  axis closer to the direction of growth, but in any case the ultrasonic data is generally consistent with the X-ray data. As with the X-ray data, there is no obvious trend in texturing as a function of cooling rate. In addition to overall slower speeds in the 10 wt.% Sn–Zn cubes (K and L), the elastic anisotropy is somewhat less, perhaps because of the increasing amount of interdendritic Sn crystallites, whose orientation is likely random (and in any case Sn is only 5% anisotropic).

For the cubes of 100% Zn (A and B), as discussed, the measured wavespeed in the growth direction depended on the position of the transducer. Fig. 8 shows that although the growth direction in 100% Zn is more commonly  $\langle 001 \rangle$ , there is one grain oriented more closely to  $\langle 210 \rangle$ , and this grain is relatively large, as is typical in 100% Zn (Figs. 6

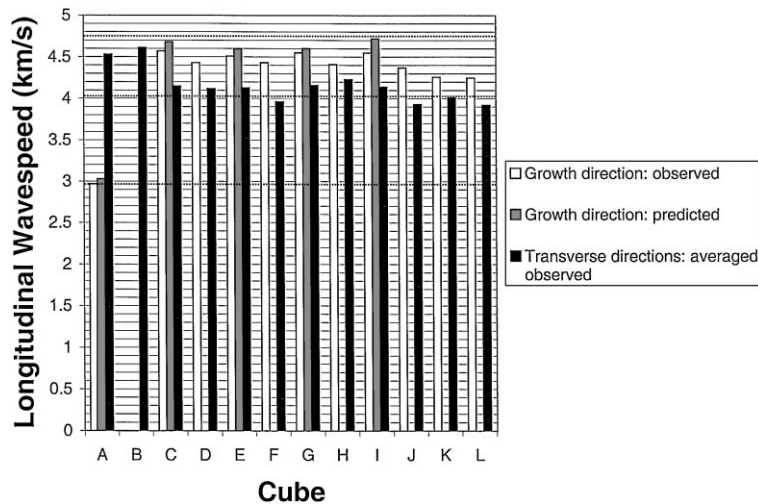


Fig. 10. Observed and predicted wavespeeds from the data given in Table 1. For a given cube the observed speeds that are plotted represent the average from multiple echoes, when available, and the average of the transverse directions. The predicted speeds are based on the direction of growth as determined by the X-ray data, as explained in the text. The horizontal dotted lines give the speeds if the solidification texturing were complete: the upper one for transverse directions in 100% Zn and the growth direction in dendritic Zn alloys (but assuming the alloy percent is not too large), the middle one for transverse directions in Zn alloys, and the lower one for the growth direction in 100% Zn. Cube A: top, 100% Zn, cooled at 1.5°C/min; Cube B: bottom, 100% Zn, 1.5°C/min; Cube C: top, 97% Zn, 0.75°C/min; Cube D: bottom, 97% Zn, 0.75°C/min; Cube E: top, 97% Zn, 1.5°C/min; Cube F: bottom, 97% Zn, 1.5°C/min; Cube G: top, 97% Zn, 1.5°C/min; Cube H: bottom, 97% Zn, 1.5°C/min; Cube I: top, 97% Zn, 2.5°C/min; Cube J: bottom, 97% Zn, 2.5°C/min; Cube K: top, 90% Zn, 1.5°C/min; Cube L: bottom, 90% Zn, 1.5°C/min.

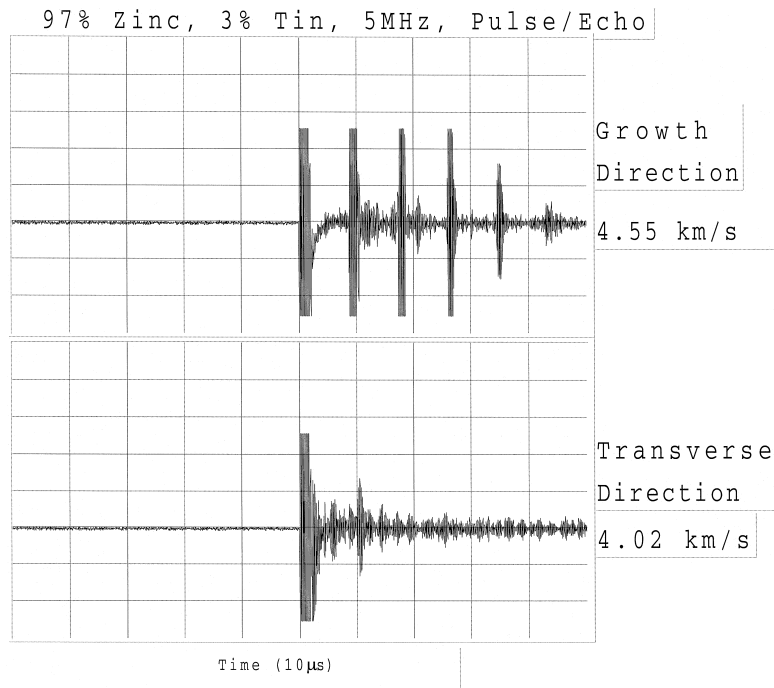


Fig. 11. Waveforms for a 5 MHz ultrasonic pulse echoing through the top cube cut from a 97% Zn ingot cooled at 1.5°C/min. Top, parallel to the growth direction; bottom, transverse to the growth direction. Each horizontal division represents 10  $\mu$ s, amplitude arbitrary. The timebase has been compressed for visualization of several echoes, the wavespeed is determined from the travel time that is picked from an expanded timebase.

and 7). Hence, since this grain has a cross-section comparable to that of the transducer, when the transducer was located directly over the grain, the measured wavespeed was nearly that of the  $\langle 210 \rangle$  direction (Table 1, in parentheses), whereas when the transducer was located away from the rogue grain, the measured wavespeed was that of the predicted slow  $\langle 001 \rangle$  direction (Table 1, without parentheses). In the transverse directions the measured speeds were less sensitive to the transducer location and were close to but less than that of the  $\langle 210 \rangle$  direction, presumably because the rays passed primarily through grains oriented with the fast, isotropic basal plane transverse to the growth direction, but were slowed somewhat by the one columnar grain with the horizontal slow  $c$ -axis.

In 100% Zn multiple echoes were clearly visible in all three directions (Fig. 12), unlike for the alloys. We believe this is because rays in directionally solidified 100% Zn do not cross as many grain boundaries with as large impedance contrasts. On the

other hand, in alloys with a solidification texture, where arbitrary rotation of grains about the growth direction leads to impedance contrasts transverse to the growth direction, an anisotropic apparent attenuation due to scattering results. This is the likely cause of the signal between primary echoes for the waveform shown in the bottom of Fig. 11. Because of the large single crystal elastic anisotropy of Zn, the scattering is severe enough to obscure primary echoes beyond the first. By holding constant the experimental variables (except perhaps for the transducer/sample bond) that make it difficult to quantify the attenuation, we can at least get a measure of the relative attenuation between different cubes and directions. Figs. 11 and 12 and a knowledge of the cubes' grain orientation distribution lead us to believe that scattering is the cause for the differing apparent attenuation anisotropy.

In these 5 MHz ultrasonic experiments, with a wavespeed between 2.9 and 4.8 km/s, the wavelength  $\lambda$  is in the range 0.58–0.96 mm. For the

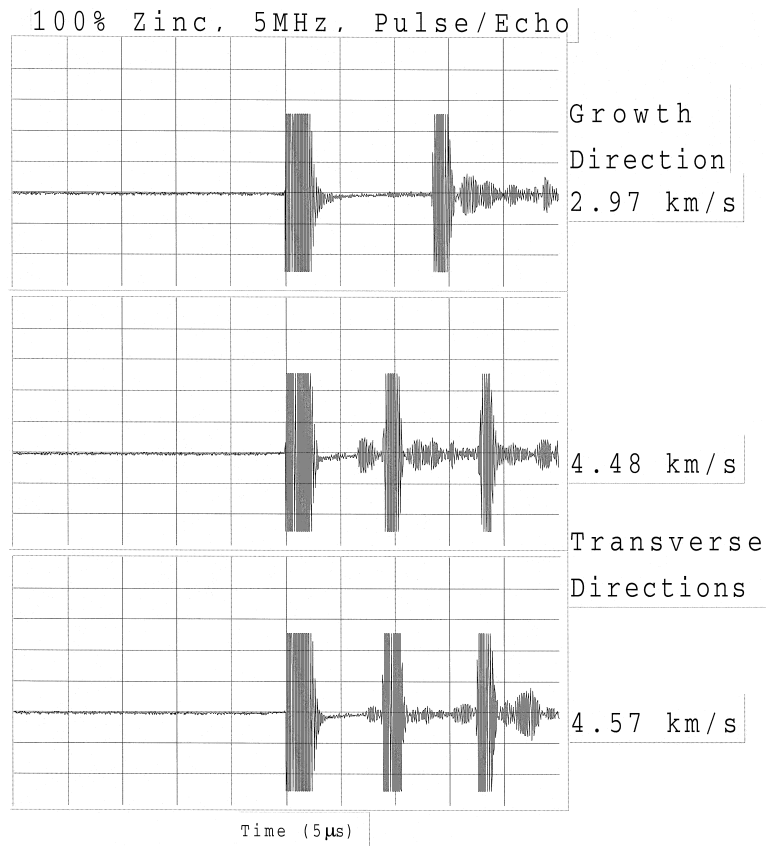


Fig. 12. As for Fig. 11, but for the top cube cut from a 100% Zn ingot cooled at 1.5°C/min. Waveforms for both transverse directions are shown. Each horizontal division is 5 μs.

alloys, the typical grain size  $d$  transverse to the growth direction is a few millimeters (Fig. 4), much longer in the growth direction. For 100% Zn, the typical transverse grain size is nearly a centimeter (Fig. 5). Thus, these experiments are perhaps neither in the reflection limit nor the Rayleigh limit, but are closer to the former.

## 5. Conclusions

In this study, we have confirmed prior work that shows that the preferred growth direction of solidified, undeformed hcp Zn alloys is  $\langle 210 \rangle$  and of pure Zn is  $\langle 001 \rangle$ . We have done this using back-reflection X-ray diffraction. Moreover, our ultrasonic results show that the crystallographic axes transverse to growth are arbitrarily oriented. If high-pressure Fe

is hcp, and if the inner core tends to grow with cylindrical rather than spherical symmetry due to a tendency for cylindrical heat flow due to the rotationally dominated pattern of outer core convection, then solidification texturing may be responsible for the observed elastic anisotropy (Bergman, 1997). In determining the importance of solidification texturing in the Earth's inner core the issues are: (1) is the pattern of heat flow sufficiently cylindrical, (2) how much does post-solidification deformation change the frozen-in texturing, and (3) what might account for longitudinal variations in the strength of the anisotropy?

Using ultrasonics we have also shown that solidification texturing can also result in an apparent attenuation anisotropy that is due to anisotropic scattering off grains oriented arbitrarily in the directions transverse to growth. In fact, apparent attenuation

anisotropy follows inevitably from solidification texturing of hcp alloys, and can naturally explain the observed inner core seismic attenuation anisotropy if the growth tends to be cylindrical and if the transverse grain size  $d$  is comparable to, or perhaps an order of magnitude smaller than, the seismic body wavelength of a few kilometers (Bergman, 1998). In the reflection limit where  $\lambda \ll d$ , as was nearly the case in our ultrasonic experiments, the transmitted energy is the product of the transmission coefficients at each boundary, each less than one. However, multiple reflections can result in forward scattering when  $\lambda$  is comparable to  $d$ . Thus, for a broadband pulse, high frequencies with  $\lambda \ll d$  are preferentially filtered out of the earliest portion of a transmitted pulse, decreasing the direct wave amplitude and broadening the pulse as the multiple reflections arrive (O'Doherty and Anstey, 1971; Richards and Menke, 1983). This stratigraphic attenuation may be observed in the inner core (Cormier et al., 1998).

Future work involving ultrasonics of directionally solidified metallic alloys will include quantifying apparent attenuation anisotropy as a function of relative wavelength and grain size, and a study of shear waves. Experiments on the effects of rotation and magnetic fields on solidification, and studies of the deformation of mushy zones, should also contribute to progress in understanding this fascinating region of the Earth.

## Acknowledgements

We would like to thank Jeremy Bloxham, Vern Cormier, David Fearn, Rick O'Connell, Frans Spaepen, and Stephen Zatman for helpful discussions, the anonymous reviewers for their suggestions, and Dan Du Vall for his help with the photography. This work was supported by the NSF and a Cottrell College Science Award of the Research Corporation.

## References

- Bergman, M.I., 1997. Measurements of elastic anisotropy due to solidification texturing and the implications for the Earth's inner core. *Nature* 389, 60–63.
- Bergman, M.I., 1998. Estimates of the Earth's inner core grain size. *Geophys. Res. Lett.* 25, 1593–1596.
- Bergman, M.I., Fearn, D.R., Bloxham, J., Shannon, M., 1997. Convection and channel formation in solidifying Pb–Sn alloys. *Metall. Trans.* 28A, 859–866.
- Bhattacharyya, J., Shearer, P., Masters, G., 1993. Inner core attenuation from short-period PKP(BC) versus PKP(DF) waveforms. *Geophys. J. Int.* 114, 1–11.
- Buffett, B., Creager, K.C., 1998. Rotation and deformation of the inner core (abstract), SEDI, Tours, France.
- Cormier, V.F., Xu, L., Choy, G.L., 1998. Seismic attenuation of the inner core: viscoelastic or stratigraphic? *Geophys. Res. Lett.* (in press).
- Creager, K.C., 1992. Anisotropy of the inner core from differential travel times of the phases PKP and PKIKP. *Nature* 356, 309–314.
- Cullity, B.D., 1978. *Elements of X-ray Diffraction*, Addison-Wesley, Reading, MA.
- Fearn, D.R., Loper, D.E., Roberts, P.H., 1981. Structure of the Earth's inner core. *Nature* 292, 232–233.
- Gow, A.J., 1986. Orientation textures in ice sheets of quietly frozen lakes. *J. Cryst. Growth* 74, 247–258.
- Hellawell, A., Herbert, P.M., 1962. The development of preferred orientations during the freezing of metals and alloys. *Proc. R. Soc. London, Ser. A* 269, 560–573.
- Jeanloz, R., Wenk, H.R., 1988. Convection and anisotropy of the inner core. *Geophys. Res. Lett.* 15, 72–75.
- Jephcoat, A., Olson, P., 1987. Is the inner core of the Earth pure iron?. *Nature* 325, 332–335.
- Karato, S.I., 1993. Inner core anisotropy due to the magnetic field-induced preferred orientation of iron. *Science* 262, 1708–1711.
- Loper, D.E., Fearn, D.R., 1983. A seismic model of a partially molten inner core. *J. Geophys. Res.* 88, 1235–1242.
- Mason, W.P., McSkimin, H.J., 1948. Energy losses of sound waves in metals due to scattering and diffusion. *J. Appl. Phys.* 19, 940–946.
- McSkimin, H.J., 1950. Ultrasonic measurement techniques applicable to small solid specimens. *J. Acoust. Soc. Am.* 22, 413–418.
- Morelli, A., Dziewonski, A.M., Woodhouse, J.H., 1986. Anisotropy of the inner core inferred from PKIKP travel times. *Geophys. Res. Lett.* 13, 1545–1548.
- O'Doherty, R.F., Anstey, N.A., 1971. Reflections on amplitude. *Geophys. Prospect.* 19, 430–458.
- Papadakis, E.P., 1968. Ultrasonic attenuation caused by scattering in polycrystalline media. In: Mason, W.P. (Ed.), *Physical Acoustics*. Academic Press, New York.
- Papadakis, E.P., 1990. The measurement of ultrasonic attenuation. In: Thurston, R.N., Pierce, A.D. (Eds.), *Physical Acoustics*. Academic Press, New York.
- Poirier, J.-P., Price, G.D., 1998. Plastic deformation and the seismic anisotropy of the inner core (abstract), SEDI, Tours, France.
- Porter, D.A., Easterling, K.E., 1992. *Phase Transformations in Metals and Alloys*, Chapman & Hall, London.
- Richards, P.G., Menke, W., 1983. The apparent attenuation of a scattering medium. *Bull. Seismol. Soc. Am.* 73, 1005–1021.

- Roth, W., 1948. Scattering of ultrasonic radiation in polycrystalline metals. *J. Appl. Phys.* 19, 901–910.
- Saxena, S.K., Dubrovinsky, L.S., Haggkvist, P., 1996. X-ray evidence for the new phase  $\beta$ -iron at high temperature and high pressure. *Geophys. Res. Lett.* 23, 2441–2444.
- Shen, G., Mao, H.K., Hemley, R.J., Duffy, T.S., Rivers, M.L., 1998. Melting and crystal structure of iron at high pressures and temperatures. *Geophys. Res. Lett.* 25, 373–376.
- Simmons, G., Wang, H., 1971. *Single Crystal Elastic Constants and Calculated Aggregate Properties*. MIT Press, Cambridge, MA.
- Smithells, C.J., 1949. *Metals Reference Book*. Interscience Publishers, New York.
- Song, X., 1997. Anisotropy of the Earth's inner core. *Rev. Geophys.* 35, 297–314.
- Song, X., Helmberger, D.V., 1993. Anisotropy of Earth's inner core. *Geophys. Res. Lett.* 20, 2591–2594.
- Souriau, A., Romanowicz, B., 1997. Anisotropy in inner core attenuation: a new type of data to constrain the nature of the solid core. *Geophys. Res. Lett.* 24, 2103–2106.
- Stixrude, L., Cohen, R.E., 1995. High-pressure elasticity of iron and anisotropy of Earth's inner core. *Science* 267, 1972–1975.
- Tromp, J., 1993. Support for anisotropy of the Earth's inner core from free oscillations. *Nature* 366, 678–681.
- Weeks, W.F., Gow, A.J., 1978. Preferred crystal orientations in the fast ice along the margins of the Arctic Ocean. *J. Geophys. Res.* 83, 5105–5121.
- Woodhouse, J.H., Giardini, D., Li, X.-D., 1986. Evidence for inner core anisotropy from free oscillations. *Geophys. Res. Lett.* 13, 1549–1552.
- Yoshida, S., Sumita, I., Kumazawa, M., 1996. Growth model of the inner core coupled with the outer core dynamics and the resulting elastic anisotropy. *J. Geophys. Res.* 101, 28085–28103.
- Yukutake, T., 1998. Implausibility of thermal convection in the Earth's solid inner core. *Phys. Earth Planet. Inter.* 108, 1–13.